communications engineering

A Nature Portfolio journal

Article

https://doi.org/10.1038/s44172-025-00402-9

A method for reconstructing the dynamic displacement of floating structures based on acceleration measurements and comparison with data-reconstruction techniques

Shujian Gao ✉, Xi Chen, Zewen Pan, Zhe Tian & Fushun Liu

Accurately measuring the dynamic response in marine structures is crucial for ensuring service safety. Here we developed a method for reconstructing the dynamic displacement of floating structures based on acceleration measurements, addressing the challenges posed by the limitations of non-contact measurement devices due to the absence of fixed reference points in marine environments. This method avoids the issues of transition and low-frequency component loss typically encountered in integration-based reconstruction methods by the precise removal of drift terms, while achieving dual improvements in both reconstruction accuracy and efficiency compared to recent methods. A comprehensive comparison is made between the proposed method and widely used displacement measurement devices in physical model testing and field applications of offshore floating structures, validating the broad potential for applications requiring structural displacement measurement in complex marine environments.

During the operation of offshore floating structures, dynamic displacement information serves as a crucial indicator of structural motion characteristics[1,2], directly reflecting operational status and service safety[3,4]. Furthermore, dynamic displacement measurement is in high demand across several fields, including structural monitoring[5,6], system identification[7,8], and so on. For example, during multi-body installation operations, accurate dynamic displacement measurement can enhance both the efficiency and precision of structural movement control[9]. In modal parameter analysis, displacement data is more effective than acceleration data for producing stable modal damping ratios[10]. Additionally, precise displacement boundary conditions are commonly required as inputs in structural transient response analysis[11]. In system identification, displacements serve as valuable inputs for generating state-space models, thereby facilitating the interpretation of physical parameters[12]. As a result, obtaining accurate dynamic displacement data for floating structures, particularly in deep-sea operational environments, has become a critical issue[13,14].

Displacement is one of the most easily convertible physical quantities. Kinematic quantities such as velocity, acceleration, and angle can be directly derived from changes in displacement, while pressure and temperature can be converted into displacement values through elastic and thermoelastic components. As a result, displacement sensors are among the most widely used sensors. Current displacement measurement devices can be classified into two categories: contact sensors and non-contact measuring devices. Non-contact structural dynamic displacement measurement devices, including total stations, laser displacement sensors, and close-range photogrammetry, have been extensively employed in displacement testing for bridge structures[15,16], building structures[17,18], tunnel engineering[19,20], and slope deformations[21,22]. Although non-contact measurement technologies offer high accuracy, achieving millimeter-level precision, they are not suitable for real marine environments, primarily due to the lack of fixed reference points.

Contact displacement sensors typically rely on measuring structural motion acceleration, using techniques such as integration, filtering, and baseline correction to reconstruct displacement[23]. However, due to technological limitations, these sensors often produce measurement errors that do not accurately reflect the true motion of the structure[24]. Given the unique challenges of the marine environment and the limitations of contact sensors, the use of Digital Global Positioning System (DGPS) technology for

Shandong Province Key Laboratory of Ocean Engineering, Ocean University of China, 266100 Qingdao, China. ✉e-mail: gaoshujian@ouc.edu.cn

displacement measurement provides a means to correct for drift displacement[25]. While this method effectively reduces drift issues in offshore structure displacement measurement, it remains vulnerable to factors such as occlusion and harsh environmental conditions, which can impact data transmission. Additionally, the accuracy of DGPS is limited, typically achieving only meter-level precision in deep-sea environments. Especially in the vertical direction, although differential systems have been used to improve the testing accuracy, the accuracy for the heave response is still insufficient compared to the horizontal direction[26]. Also, data can suffer from issues like jumps[27], drift[28], instability, and even complete loss[29]. These challenges can lead to structural misalignment or cause the structure to be driven to an incorrect position. As a result, multiple offshore platform accidents have been attributed to errors in motion displacement testing[30].

In addition to employing DGPS technology to correct the integral displacement of offshore structures, technological advancements have been made in reconstructing motion displacement from measured acceleration. While there is a strict theoretical relationship between acceleration and displacement through integration, actual sea conditions introduce several challenges, such as the unknown initial motion state, environmental noise, sensor baseline offsets, and other factors, leading to drift during the integration process. This drift leads to inaccuracies in the reconstructed motion displacement, failing to accurately reflect the true state of structures[31]. Currently, approaches for reconstructing motion displacement from acceleration include filtering techniques[32–34], baseline correction techniques[35,36], and polynomial fitting techniques[37,38]. Low-frequency drift, a common cause of integration errors, can be mitigated through high-pass filtering applied to the integrated displacement. However, for offshore floating structures, which exhibit low-frequency motion, filtering approaches may not only eliminate the drift components, but also lead to the loss of real motion response components. This limitation is particularly problematic when dealing with issues under complex marine conditions. Furthermore, challenges related to the transition section and initial parameter selection also contribute to errors in displacement reconstruction[39]. Baseline correction approaches, commonly used in seismic response analysis, fit the baseline of the integrated data; however, it merely fits the baseline of the integration result and fails to capture detailed information regarding the structural motion response. This limitation results in errors when applied to offshore structures subject to complex noise conditions. Polynomial-based approaches, which remove drift terms by fitting integrated drift displacement with polynomials, are inadequate for floating structures that exhibit strong nonlinear behavior. Additionally, Liu et al.[40,41] proposed a non-integral displacement reconstruction approace that achieves high-precision reconstruction for fixed offshore structures. However, this approach relies on fitting the acceleration using a state-space model. When applied to the displacement reconstruction of offshore floating structures, it encounters challenges such as limited processing of long-term signals and reduced analysis efficiency.

To enhance the long-term stability and high-precision measurement of displacement in offshore floating structures, this paper proposes a displacement reconstruction method based on the precise removal of integral drift terms. The method is compared with widely used displacement testing devices and reconstruction approaches across several key performance aspects. The comparison reveals three contributions of the proposed method: (1) Under experimental conditions, the proposed method effectively addresses data loss issues encountered by traditional non-contact optical devices, which are influenced by environmental light and the limited range of structural motion amplitude; (2) In practical marine environments, the proposed method overcomes the challenge of missing fixed reference points for non-contact devices; (3) Compared to traditional approaches, this method not only improves computational accuracy but also enhances calculation efficiency.

Methods

Accurately obtaining the motion response of floating structures is crucial for their safe operation, especially under the combined influence of a complex marine environment, mooring systems, risers, and other auxiliary structures. Acceleration is the most easily obtainable and reliable physical quantity for measuring offshore structures, facilitating the reconstruction of other physical quantities. However, two key challenges arise: (1) How to achieve normalized characterization of the motion response with drift terms after integration? (2) How to accurately identify and remove these drift terms? As shown in Eqs. (2) and (3), both velocity and displacement obtained through integration share these issues, though the displacement is more complex after integration. The following derivation uses the integrated displacement as an example for analysis. The proposed method is universal and also applicable to velocity-related issues; however, details will not be provided here. The scheme of the proposed method can be found in Supplementary Fig. 2.

Drift displacement after integration

Marine structures are subjected to complex impact during service, including forces from mechanical equipment and various environmental factors such wind, waves, and currents. As a result, the measured acceleration includes not only the actual structural vibration or motion but also several additional components: harmonic components generated by equipment operation (denoted as $h(t)$), transient attenuation components due to ship impact or ice-induced load (denoted as $a(t)$), slow variation components caused by tidal range changes (denoted as $v(t)$), and other complex noise components. This can be described as

$$\ddot{x}(t) = \overline{\ddot{x}}(t) + h(t) + a(t) + v(t) + n_s(t) + n_e(t) + b \tag{1}$$

where $\overline{\ddot{x}}(t)$ and $\ddot{x}(t)$ represent the actual and measured structural accelerations, respectively. b denotes the baseline bias of the accelerometer. $n_s(t)$ represents sensor noise components that affect data quality but not cause structural movement, while $n_e(t)$ refers to noise components in the marine environment that interfere with structural movement.

In theory, the structural velocity can be calculated by integrating the measured acceleration:

$$\begin{aligned}\dot{x}(t) &= \int_0^t \ddot{x}(\tau)\mathrm{d}\tau + \dot{x}(0)\\ &= \int_0^t [\overline{\ddot{x}}(\tau) + h(\tau) + a(\tau) + v(\tau) + n_s(\tau) + n_e(\tau) + b]\,\mathrm{d}\tau + \dot{x}(0)\\ &= \int_0^t [\overline{\ddot{x}}(\tau) + n_e(\tau)]\,\mathrm{d}\tau + \int_0^t [h(\tau) + a(\tau) + v(\tau) + n_s(\tau)]\,\mathrm{d}\tau + \dot{x}(0) + bt\end{aligned} \tag{2}$$

where $\dot{x}(0)$ represents the initial velocity of the structure at the start of the test. It is clear that the integration process introduces two unexpected components in the calculated velocity: one is the mean deviation caused by the initial velocity $\dot{x}(0)$, and the other is the linear drift term b resulting from the baseline bias of the accelerometer. It is worth noting that the term b is more complex in real measurements and may vary with time (i.e., $b(t)$ in theory). However, because it typically represents a very low-frequency variation, it is often simplified as b for clearer formula derivation.

The structural displacement can then be calculated through the integral process as follows:

$$\begin{aligned}x(t) &= \int_0^t \dot{x}(\tau)\mathrm{d}\tau + x(0)\\ &= \int_0^t \{\int_0^t [\overline{\ddot{x}}(\tau) + n_e(\tau)]\,\mathrm{d}\tau + \int_0^t [h(\tau) + a(\tau) + v(\tau) + n_s(\tau)]\,\mathrm{d}\tau + \dot{x}(0) + bt\}\,\mathrm{d}\tau + x(0)\\ &= \int_0^t \int_0^t [\overline{\ddot{x}}(\tau) + n_e(\tau)]\,\mathrm{d}\tau\mathrm{d}\tau + \int_0^t \int_0^t [h(\tau) + a(\tau) + v(\tau) + n_s(\tau)]\,\mathrm{d}\tau\,\mathrm{d}\tau + x(0) + \dot{x}(0)t + \frac{1}{2}bt^2\\ &= x^{real}(t) + x^{noise}(t) + x^{drift}(t)\end{aligned} \tag{3}$$

where $x(0)$ represents the initial displacement at the start of the measurement. It should be noted that the integrated displacement consists of three parts: $x^{real}(t) = \int_0^t [\overline{\ddot{x}}(\tau) + h(\tau) + a(\tau) + v(\tau) + n_e(\tau)]\,\mathrm{d}\tau$ represents the true structural dynamic displacement; $x^{noise}(t) = \int_0^t \int_0^t [h(\tau) + a(\tau) + v(\tau) + n_s(\tau)]\,\mathrm{d}\tau\,\mathrm{d}\tau$ represents the noise influence from various factors, and $x^{drift}(t) = x(0) + \dot{x}(0)t + \frac{1}{2}bt^2$ represents the drift terms. The terms $\dot{x}(0)t$ and $\frac{1}{2}bt^2$ account for the influences of the initial velocity and the baseline bias of the accelerometer, resulting in linear and exponential drift trends in the integral results. Additionally, $x(0)$ represents the influence of the initial displacement, which leads to a constant deviation.

Accurate characterization of the integrated-displacement

The primary challenge, as shown in Eq. (3), lies in effectively extracting the drift term $x^{drift}(t)$. Removing this drift term would isolate the real displacement. However, estimating and extracting $x^{drift}(t)$ is challenging, because it is not purely harmonic. Traditional signal decomposition methods, such as Fourier and wavelet decomposition[42,43], which represent signals as sums of sine or cosine functions, are not suitable for this extraction. To account for the various characteristics of the structural motion response, $x(t)$ is expressed as follows:

$$\begin{aligned} x(t) &= x^{real}(t) + x^{noise}(t) + x^{drift}(t) \\ &= \sum_{d=1}^{N_d} A_d e^{i\theta_d} e^{(-\xi_d + i\omega_d)t} + \sum_{n=1}^{N_n} A_n e^{i\theta_n} e^{(-\xi_n + i\omega_n)t} + \sum_{r=1}^{N_r} A_r e^{i\theta_r} e^{(-\xi_r + i\omega_r)t} \\ &= \sum_{j=1}^{N_j} A_j e^{i\theta_j} e^{(-\xi_j + i\omega_j)t} \end{aligned} \tag{4}$$

where N_r, N_n, and N_d denote the number of the components in the true displacement, noise terms, and drift terms, respectively, with $N_j = N_r + N_n + N_d$. The variables $A_{(.)}$, $\theta_{(.)}$, $\xi_{(.)}$, and $\omega_{(.)}$ represent the amplitude, phase, damping ratio, and angular frequency of the corresponding components. The following relationships are defined:

$$\begin{cases} \alpha_j = A_j e^{i\theta_j} \\ \beta_j = -\xi_j + i\omega_j \end{cases} \tag{5}$$

Consequently, the real part of α_j represents the amplitude of the component, while the imaginary part of β_j corresponds to the component's frequency, as expressed in the following equation:

$$\begin{cases} A_j = Re(\alpha_j) \\ \omega_j = 2\pi f_j = Im(\beta_j) \end{cases} \tag{6}$$

where f_j denotes the frequency of the corresponding component, and $Re(.)$ and $Im(.)$ represent the real and imaginary parts, respectively. Therefore, when α_j and β_j are accurately estimated, the drift terms can be effectively removed using the corresponding component's frequency and amplitude.

Solution to the characterization parameters

In Eq. (4), the exponential functions $e^{(-\xi_j + i\omega_j)t}$ forms a basis on the open interval $0 < t < T$, and the variables α_j and β_j in Eq. (5) can be interpreted as the general solutions to pth-order ordinary differential homogeneous linear equations, characterized by the coefficients a_j, as follows:

$$\sum_{j=1}^{N_j} a_j \frac{d^j x}{dt^j}(t) = \sum_{j=1}^{N_j} a_j x^{(j)}(t) = 0 \tag{7}$$

However, the polynomial root-finding process for Eq. (7) is highly sensitive to errors due to its poor numerical conditioning, which can lead to inaccurate parameter estimation, especially in the presence of noise interference. This is often a critical issue when analyzing the dynamic responses of offshore floating structures. To address this issue, the proposed method introduces Eq. (8) as

$$\tilde{x}_1 = x^{(0)}, \tilde{x}_2 = x^{(1)}, \tilde{x}_3 = x^{(2)}, \ldots, \tilde{x}_{N_j-1} = x^{(N_j-2)}, \tilde{x}_{N_j} = x^{(N_j-1)} \tag{8}$$

and Eq. (7) can be transformed into a first-order matrix differential equation as follows:

$$\begin{Bmatrix} \frac{d\tilde{x}_1}{dt} \\ \frac{d\tilde{x}_2}{dt} \\ \frac{d\tilde{x}_3}{dt} \\ \vdots \\ \frac{d\tilde{x}_{N_j-1}}{dt} \\ \frac{d\tilde{x}_{N_j}}{dt} \end{Bmatrix} = \begin{bmatrix} 0 & 1 & 0 & 0 & \cdots & 0 & 0 \\ 0 & 0 & 1 & 0 & \cdots & 0 & 0 \\ 0 & 0 & 0 & 1 & \cdots & 0 & 0 \\ \vdots & \vdots & \vdots & \vdots & \ddots & \vdots & \vdots \\ 0 & 0 & 0 & 0 & \cdots & 0 & 1 \\ -a_0 & -a_1 & -a_2 & -a_3 & \cdots & -a_{N_j-2} & -a_{N_j-1} \end{bmatrix} \begin{Bmatrix} \tilde{x}_1 \\ \tilde{x}_2 \\ \tilde{x}_3 \\ \vdots \\ \tilde{x}_{N_j-1} \\ \tilde{x}_{N_j} \end{Bmatrix} \tag{9}$$

where a_{N_j} is commonly set to 1 for generality. Theoretically, the N_j eigenroots of the matrix formed by the coefficients $a_.$ in Eq. (9) correspond to the N_j roots of the eigenpolynomial in Eq. (7). Therefore, a Hankel matrix can be defined as

$$\mathbf{H}_{\tilde{x}}(j) = \begin{bmatrix} \tilde{x}_j & \tilde{x}_{j+1} & \cdots & \tilde{x}_{j+\eta-1} \\ \tilde{x}_{j+1} & \tilde{x}_{j+2} & \cdots & \tilde{x}_{j+\eta} \\ \vdots & \vdots & \ddots & \vdots \\ \tilde{x}_{j+\xi-1} & \tilde{x}_{j+\xi} & \cdots & \tilde{x}_{j+\xi+\eta-2} \end{bmatrix} \in \mathbb{R}^{\xi\times\eta} \tag{10}$$

where η and ξ represent the selected number of rows and columns, respectively. Corresponding to the three parts in Eq. (4), the singular value decomposition is applied, allowing $\mathbf{H}(0)$ to be rewritten as follows:

$$\begin{aligned} \mathbf{H}_{\tilde{x}}(0) &= [\,\mathbf{U}^d_{mo1} \quad \mathbf{U}^r_{mo2} \quad \mathbf{U}^n_{mo3} \quad \widetilde{\mathbf{U}}_{mo4}\,] \begin{bmatrix} \mathbf{S}^d_{mo1} & \mathbf{0} & \mathbf{0} & \mathbf{0} \\ \mathbf{0} & \mathbf{S}^r_{mo2} & \mathbf{0} & \mathbf{0} \\ \mathbf{0} & \mathbf{0} & \mathbf{S}^n_{mo3} & \mathbf{0} \\ \mathbf{0} & \mathbf{0} & \mathbf{0} & \mathbf{0} \end{bmatrix} \begin{bmatrix} (\mathbf{V}^d_{mo1})^T \\ (\mathbf{V}^r_{mo2})^T \\ (\mathbf{V}^n_{mo3})^T \\ (\widetilde{\mathbf{V}}_{mo4})^T \end{bmatrix} \\ &= \mathbf{U}^d_{mo1}\mathbf{S}^r_{mo1}(\mathbf{V}^n_{mo1})^T + \mathbf{U}^d_{mo2}\mathbf{S}^r_{mo2}(\mathbf{V}^n_{mo2})^T + \mathbf{U}^d_{mo3}\mathbf{S}^r_{mo3}(\mathbf{V}^n_{mo3})^T = \mathbf{U}_{\widetilde{mo}}\mathbf{S}_{\widetilde{mo}}\mathbf{V}^T_{\widetilde{mo}} \end{aligned} \tag{11}$$

where T denotes the transpose of a vector, and $mo1$, $mo2$, and $mo3$ correspond to the model orders for drift terms, real dynamic displacement terms, and noise terms, respectively. Additionally, $\widetilde{mo} = mo1 + mo2 + mo3$ represents the total number of non-zero singular values. The singular vectors $\mathbf{U}_{\widetilde{mo}}$ and $\mathbf{V}_{\widetilde{mo}}$ have dimensions of $\eta \times \widetilde{mo}$ and $\widetilde{mo} \times \xi$, while $\mathbf{S}_{\widetilde{mo}}$ has a dimension of $\widetilde{mo} \times \widetilde{mo}$. The singular values $\mathbf{S}_{\widetilde{mo}}$ are assumed to be zero when the rank of the matrix is exceeded $\widetilde{mo}$. In theory, the model order $\widetilde{mo}$ is equal to the number of non-zero singular values shown in Eq. (11). It is important to note that due to noise interference and computational errors, the singular value corresponding to $mo4$ may not be zero, but it is typically very small. To ensure the inclusion of all N_j singular values, the dimensions of $\mathbf{H}_{\tilde{x}}(0)$ must be selected such that η and ξ are at least N_j.

According to realization theory, a relationship between $\mathbf{H}_{\tilde{x}}(0)$ and $\mathbf{H}_{\tilde{x}}(1)$ can be established by substituting $j = 1$ into Eq. (10), as follows:

$$\mathbf{H}_{\tilde{x}}(1) = \mathbf{U}_{mo}\mathbf{S}_{mo}{}^{1/2}\mathbf{P}\mathbf{S}^{1/2}_{mo}(\mathbf{V}_{mo})^T \tag{12}$$

where $\mathbf{P}$ represents the state matrix. Its realization can be estimated through matrix multiplication as follows:

$$\mathbf{P} = \mathbf{S}_{mo}{}^{-1/2}\mathbf{U}^T_{mo}\mathbf{H}_{\tilde{x}}(1)\mathbf{V}_{mo}\mathbf{S}^{-1/2}_{mo} \tag{13}$$

According to the mathematical relationship, the eigenroot of the matrix **P** is given by $e^{\beta_j \Delta t}$, allowing for the calculation of the frequency and damping ratio of each component using Eq. (5). Furthermore, Eq. (4) can be expressed as

$$\begin{bmatrix} e^{\beta_1} & e^{\beta_2} & \cdots & e^{\beta_{N_j}} \\ e^{\beta_1 \Delta t} & e^{\beta_2 \Delta t} & \cdots & e^{\beta_{N_j} \Delta t} \\ \vdots & \vdots & \ddots & \vdots \\ e^{\beta_1 (N_k-1)\Delta t} & e^{\beta_2 (N_k-1)\Delta t} & \cdots & e^{\beta_{N_j} (N_k-1)\Delta t} \end{bmatrix} \begin{Bmatrix} A_1 e^{i\theta_1} \\ A_2 e^{i\theta_2} \\ \vdots \\ A_{N_j} e^{i\theta_{N_j}} \end{Bmatrix} = \begin{Bmatrix} x_0 \\ x_1 \\ \vdots \\ x_{N_k-1} \end{Bmatrix} \tag{14}$$

and the amplitude and phase can be estimated using the least squares algorithm.

Drift terms removal and displacement reconstruction

Once the parameters for angular frequencies ω_j and amplitudes A_j are estimated, the frequencies of each component can be calculated using Eq. (6) as follows:

$$\widetilde{f}_j = \frac{Im(\beta_j)}{2\pi} = \frac{\omega_j}{2\pi}, \ where \ j = 0, 1, 2, ..., N_j \tag{15}$$

Since the frequencies of the drift terms in the displacement are theoretically zero or much smaller than those of the actual dynamic components, these drift terms can be eliminated by setting a frequency screening boundary F_s as follows:

$$|\widetilde{f}_j| \le F_s \tag{16}$$

For terms that cause drift, their frequency is usually low, close to 0. After this frequency screening step, the N_d components corresponding to the drift terms will be removed, leaving only the components that represent the actual dynamic behavior of the structure. These remaining components can then be used to reconstruct the actual dynamic displacement as follows:

$$\widetilde{x}^{real}(t) = \sum_{n=1}^{N_n} A_n e^{i\theta_n} e^{(-\xi_n + i\omega_n)t} + \sum_{r=1}^{N_r} A_r e^{i\theta_r} e^{(-\xi_r + i\omega_r)t} \tag{17}$$

Results and discussion

Application to a numerical semi-submersible platform

This section presents a case study using a semi-submersible platform simulated using Orcaflex software to obtain the 6 DOF motion response of the structure under irregular wave conditions. The calculation process is demonstrated, and the accuracy of the proposed method for reconstructing the motion displacement of marine structures is validated. Furthermore, the results from the proposed method are compared with those from traditional methods, including baseline correction, filtering, polynomial fitting, and non-integral approaches. The comparison evaluates computational accuracy, efficiency, and robustness, highlighting the advantages of the proposed method.

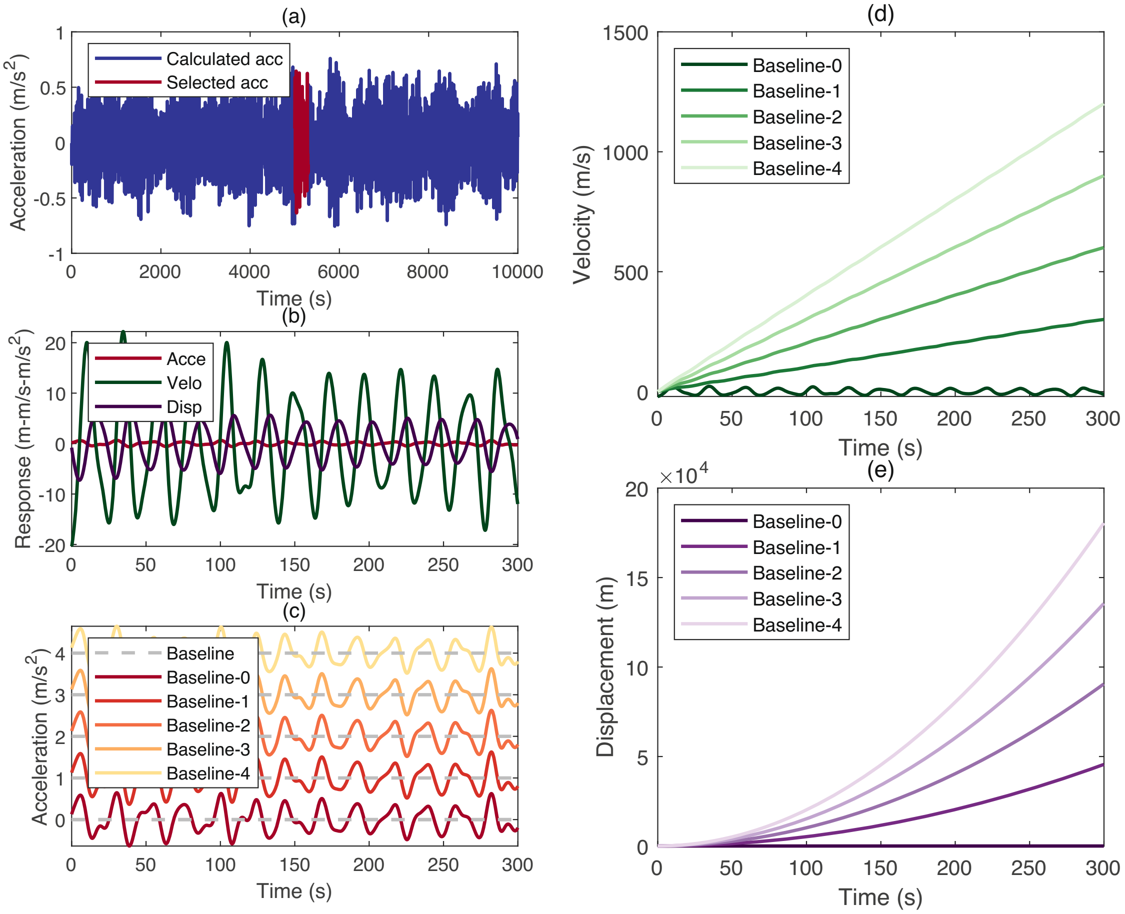

Fig. 1 | Simulated response and the integrated results. Calculated (**a**) acceleration, (**b**) velocity and displacement by Orcaflex; (**c**) Simulated acceleration with baseline bias; Comparison of integrated (**d**) velocity and (**e**) displacement with different baseline bias.

Introduction to the used numerical semi-submersible platform. The numerical model of the platform-mooring coupling system established in this study is shown in Supplementary Fig. 3. The platform is symmetrical designed along both the *x*-axis and *y*-axis, and consists of a floating hull and supporting columns. The main structure measures 124.21 m in length, 89 m in width, and has a main deck height of 45.30 m. The floating hull itself has dimensions of 124.21 m in length, 20.50 m in width, and 11.50 m in height, while the columns are 20.50 m long, 25.00 m wide, and 19.25 m high. The platform has a draft of 23 m, a displacement of 74,270.8 t, and is designed for a working depth of 1500 m.

The mooring system consists of four groups, each spaced 90 degrees apart. Within each grout, two mooring lines are arranged at 22.5 degrees intervals. Each group is equipped with two cables, symmetrically positioned along the axis. The cable properties include a wet weight of 61.20 kg m^{-1}, dry weight of 72.60 kg m^{-1}, and an axial stiffness is 8.38 N. The cable has a diameter of 127 mm, an inertia coefficient of 2.0, a resistance coefficient of 1.8, and a minimum breaking force of 13,160 kN. The positions of the fairleads and anchor points are listed in Supplementary Table 1.

Displacement reconstruction process of the proposed method. The environmental parameters used in this section correspond to the maximum sea conditions for structural operation, with a significant wave height of H_s = 12.1 m and a spectral period of T_p = 8.4 s. The calculated structural heave acceleration over a total of 3 hours from Orcaflex is illustrated in Fig. 1(a). During the calculation process, the Newmark-β algorithm and the concentrated mass method are used to calculate the responses of the platform and mooring lines, respectively. To clarify the analysis process of the proposed method and facilitate comparison with traditional methods, a 300 s segment of acceleration data (from 5000 to 5300 s) was selected for further analysis. This segment, along with its corresponding velocity and displacement, is shown in Fig. 1b. This selection implies that the initial velocity and displacement corresponding to the selected acceleration during the displacement reconstruction process are unknown without reference to the calculated answer. To fully address the baseline bias issue of the acceleration sensor typically encountered in field tests, multiple baseline bias scales have been established. The resulting acceleration data with these bias are shown in Fig. 1c, where Baseline-0 represents the original acceleration, and Baseline-1, Baseline-2, Baseline-3, and Baseline-4 represent the acceleration with bias of 1 m/s^2, 2 m/s^2, 3 m/s^2, and 4 m/s^2. Then, the effects of unknown initial velocity, unknown initial displacement, and baseline drift on the integral results are examined, as shown in Fig. 1d, e. The figures illustrate the outcomes of the first and second integrals of the selected acceleration, respectively. It is evident that, due to the unknown initial motion state of the structure (including initial velocity and displacement) and the influence of sensor baseline bias, the first integration yields a linear drift trend, while the second integration results in an exponential drift. Furthermore, as the baseline drift's influence increases, the drift amplitude becomes larger.

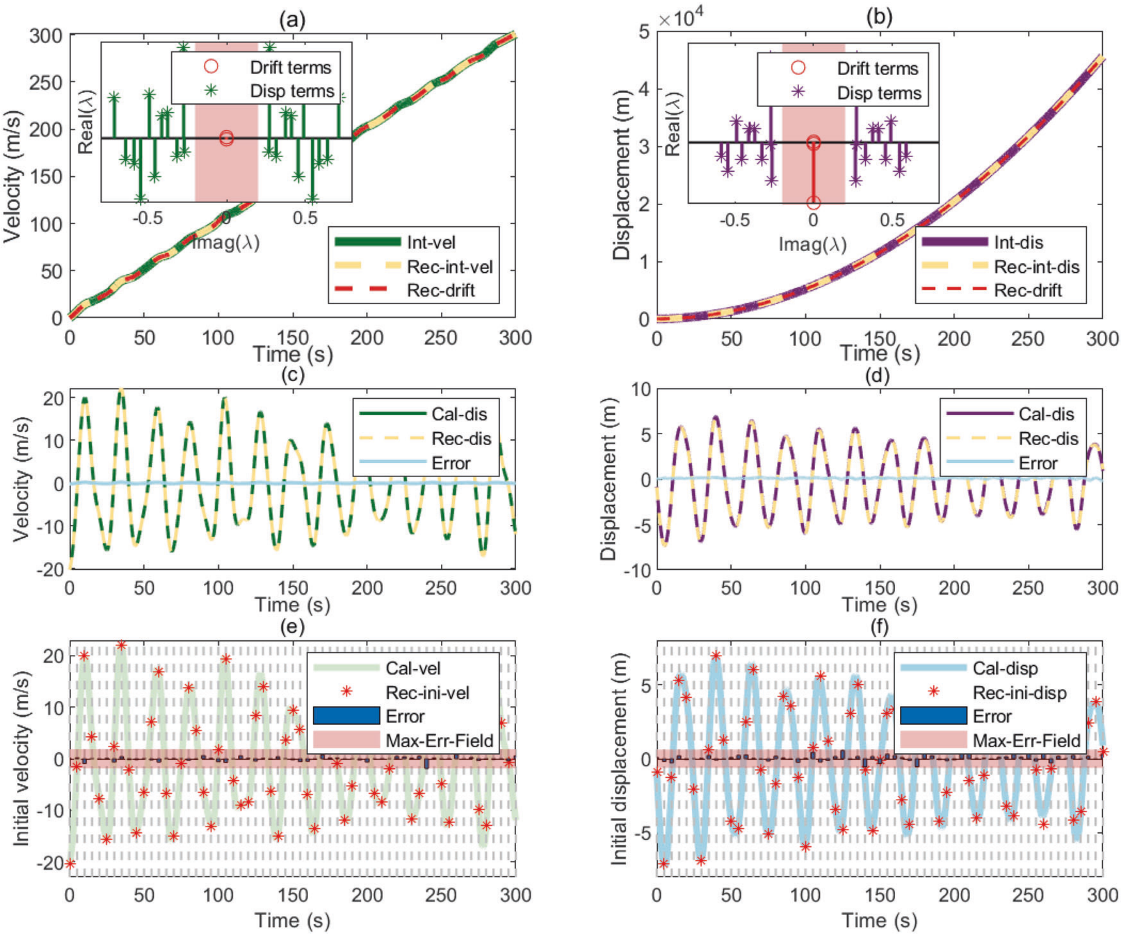

Fig. 2 | Reconstructed velocity and displacement by the proposed method. Comparison of the reconstructed results of the integrated (**a**) velocity and (**b**) displacement; Comparison of the reconstructed (**c**) velocity and (**d**) displacement with the calculated results by Orcaflex; Estimated initial (**e**) velocity and (**f**) displacement by the proposed method.

Next, to test the validity of the proposed method, the acceleration data influenced by Baseline-1, shown in Fig. 1a, was used as an example to reconstruct the real velocity and displacement of the structure. First, Eq. (4) was employed to characterize the displacement after two integrations, taking into account the effects of Baseline-1, as shown in Fig. 1e. Subsequently, the parameters α and β were solved, yielding 12 pairs of conjugate parameters, which are illustrated in the inset of Fig. 2b. The pink shaded areas highlight the frequency range below 0.1 Hz, which represent the frequency screening boundary. When the estimated α and β values were arranged in ascending order of frequency, the first two pairs were found to be $[-0.0005 + 0.0000i, -0.0005 - 0.0000i]$ and $[0.0003 + 0.0004i, 0.0003 - 0.0004i]$, corresponding to frequencies of 0 Hz and 0.0001 Hz, respectively. These values fall within the red region, indicating that they represent drift caused by baseline bias and integration effects. The remaining components, marked by purple asterisk (*), correspond to the actual dynamic displacement of the structure, can be used to reconstruct the actual dynamic displacement using Eqs. (17) and (6), as shown in Fig. 2d. The results show that the reconstructed displacement aligns closely with the real displacement calculated by Orcaflex, confirming the accuracy and validity of the proposed method.

In addition to reconstructing the time-domain curve, accurately estimating the initial displacement is crucial for practical applications. Using the proposed method, the estimated initial displacement is -0.8100 m, while Orcaflex calculates it as -0.8821 m, demonstrating good consistency between the two results. To further validate the method, the 300-s signal was truncated at various intervals (e.g., from 5 to 300 s, 10 to 300 s, 15 to 300 s). Each truncated segment was then reconstructed independently. The estimated initial displacement for each truncated signal is marked with red asterisks * in Fig. 2(f). The blue bar chart shows the error between the estimated initial displacement and the actual truncated value. The results indicate that the estimated error remains within 6%, demonstrating the high precision of the initial displacement estimation. Similarly, Fig. 2(a), (c), and present the velocity reconstruction process using the proposed method, along with the corresponding estimated initial velocities. The reconstructed velocities closely match those calculated by Orcaflex, with the estimated error for initial velocity being less than 10%. These findings confirm that the proposed method achieves high-precision velocity reconstruction and accurate initial velocity estimation.

Comparison of the reconstructed results with traditional approaches. To illustrate the advantages of the proposed method over traditional approaches, this section compares the results obtained from four conventional approaches: baseline correction, filtering, polynomial fitting, and non-integral reconstruction. The baseline-correction approach employs second-order polynomial fitting to address the drift issue[44]. The filtering-based approach applies a third-order Butterworth filter, with a normalized cutoff frequency set to 0.006[45]. In the polynomial-based approach, third-order Chebyshev polynomials are used for fitting[46]. The non-integral reconstruction approach employs a modal order of 60 for signal reconstruction[47,48]. In the following analysis, symbols of Poly, Base, Filt, and Non-I are used to represent the reconstructed results of the previous traditional methods. The results of the reconstructed displacements in both the time and frequency domains are shown in Fig. 3a, b, respectively. From the analysis, it is evident that while all four approaches provide similar results in the frequency domain, there are noticeable discrepancies in the time domain. Specifically, the baseline correction and non-integral reconstruction approaches exhibit better performance. In contrast, the polynomial fitting and filtering-based approaches not only

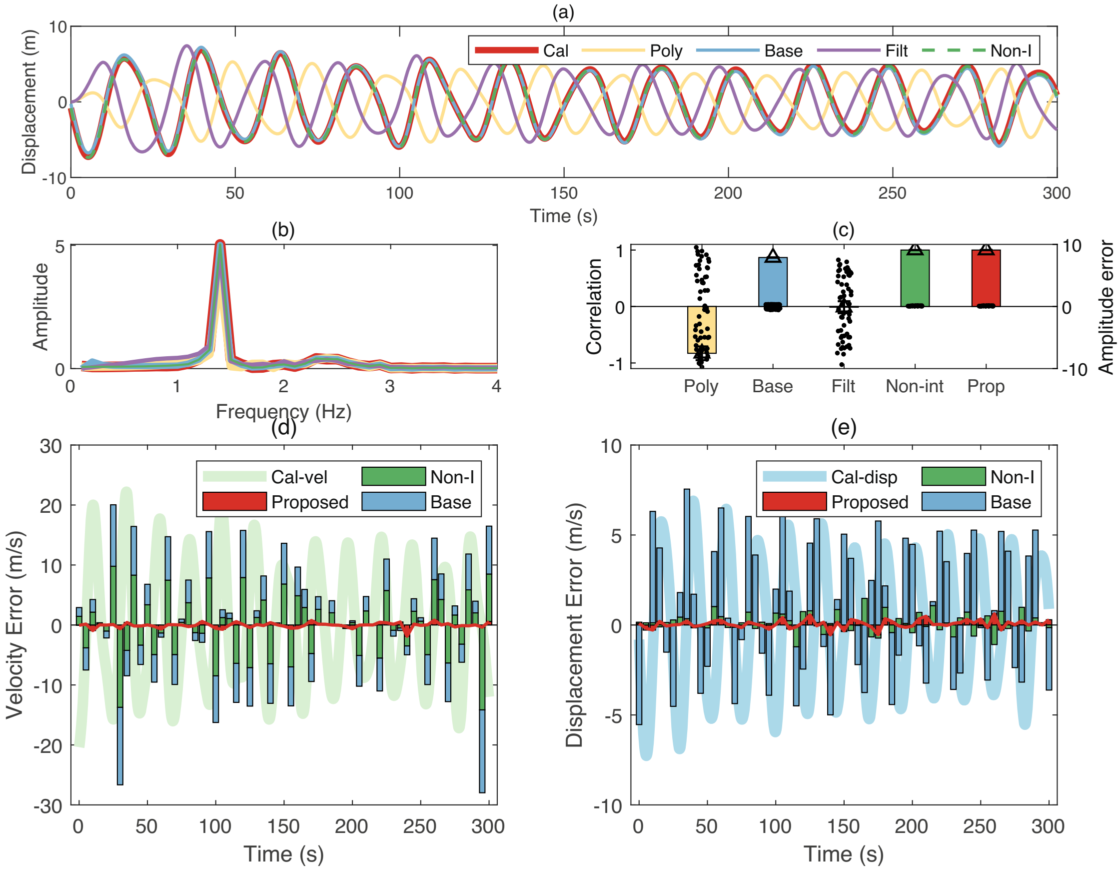

Fig. 3 | Comparison of reconstructed displacement using different approaches. Comparison in the (**a**) time and (**b**) frequency domains. (**c**) Correlation analysis. Estimated (**d**) initial velocity and (**e**) initial displacement.

show phase errors but also suffer from increased inaccuracies, particularly due to the presence of transition segments.

To quantitatively assess the effectiveness of the various displacement reconstruction approaches, two key metrics are introduced: the cross-correlation coefficient and the maximum normalization error. The cross-correlation coefficient is used to evaluate the similarity between the reconstructed displacement and the calculated response. It is defined as

$$\rho = \left| \frac{1}{N_k - 1} \sum_{i=1}^{N_k} \left(\frac{x_c(i) - \overline{x_c}}{\sigma_{x_c}} \right) \left(\frac{x_r(i) - \overline{x_r}}{\sigma_{x_r}} \right) \right| \tag{18}$$

where $x_c(t)$ and $x_r(t)$ represent the calculated and reconstructed displacements. σ_{x_c} and σ_{x_r} are the standard deviations of the calculated and reconstructed displacements, respectively. $\overline{x_c}$ and $\overline{x_r}$ are the averages of the calculated and reconstructed displacements. The value of ρ ranges from 0 to 1, where values close to 0 indicate low correlation, and values close to 1 indicate a high correlation.

The maximum normalization error quantifies the difference in amplitude between the calculated and reconstructed displacements. It is defined as

$$\eta = \left| \frac{\max[x_c(t_i) - x_r(t_i)]}{\max[x_c(t_i)]} \right| \tag{19}$$

A smaller η value indicates a smaller normalization error between the amplitudes of the two displacements. The quantitative analysis results, shown in Fig. 3c, reveal that due to the existence of phase error, the Polynomial-based approach yields a negatively correlated result, while the correlation coefficient for the Filter-based approach is close to 0. In contrast, the baseline correction approach, the non-integral approach, and the proposed method exhibit better correlation, with their correlation coefficients being 0.8974, 1.0000, and 1.0000, respectively. Furthermore, the maximum normalization error analysis indicates that both the Non-Integral approach and the proposed method produced more accurate results than the other approaches.

Similarly, truncation analysis was performed to compare the estimated errors of initial velocity and initial displacement across the various methods. Due to the inherent transition segments and truncation issues in the filtering and polynomial fitting processes, the initial parameters calculated by these approaches consistently started from zero (as shown in Fig. 3a), making further comparisons with these approaches irrelevant. The error analysis results of the estimated initial parameters from the Baseline-correction approach, the Non-Integral approach, and the proposed method are shown in Fig. 3d, e. These results demonstrate that the initial parameters estimated by the proposed method exhibit higher accuracy compared to the traditional methods, highlighting the effectiveness and reliability of the proposed approach in accurately reconstructing motion responses.

Robust analysis of different methods. In general, noise in acceleration is considered as an unwanted signal that interferes with the true structural acceleration signal. As a result, the presence of noise can cause discrepancies between the reconstructed displacement and the actual displacement when using acceleration data for displacement reconstruction. The effect of noise makes the true acceleration of the tested structure unknown. There are various sources of noise that can affect acceleration,

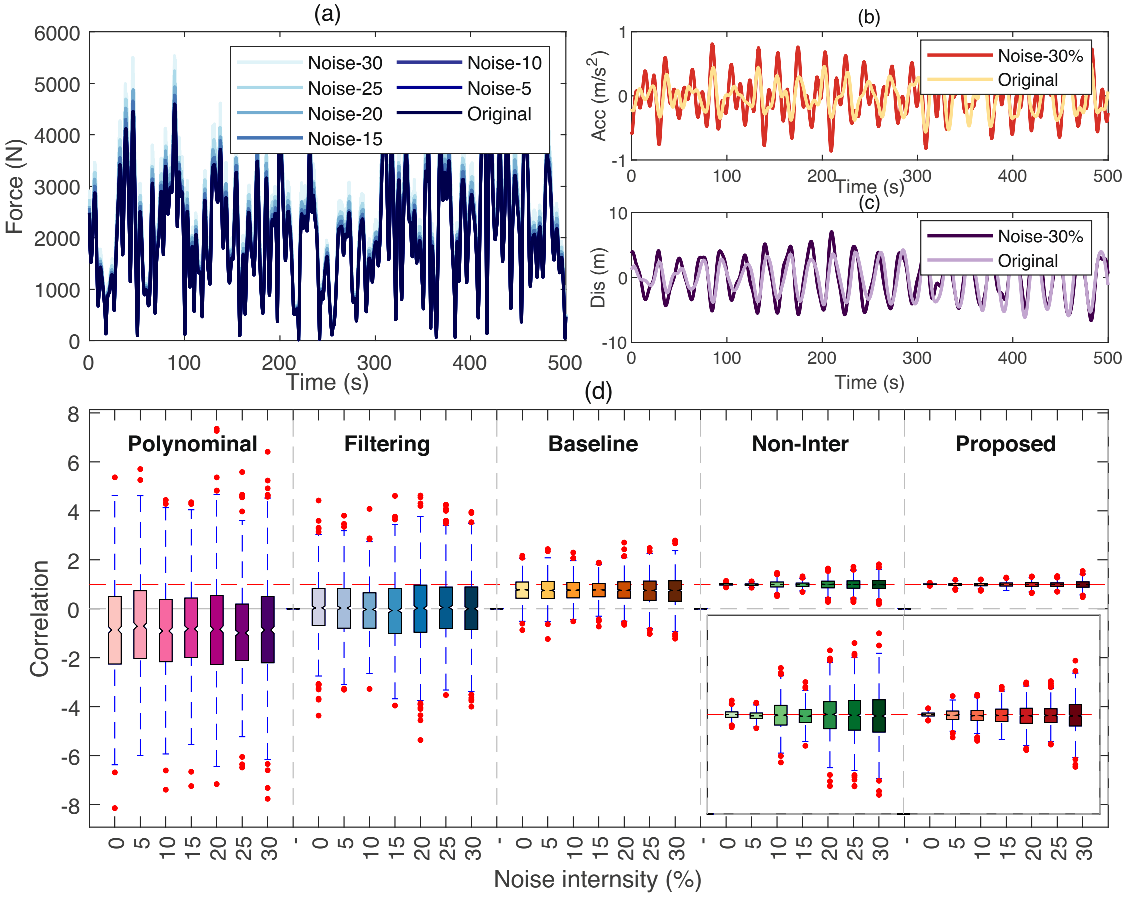

Fig. 4 | Displacement reconstruction under the first noise interference condition. **a** Wave forces acting on structures influenced by varying noise levels. Comparison of the calculated (**b**) acceleration and (**c**) displacement under 0% and 30% noise levels. **d** Quantitative evaluation results of displacement reconstructed by different approaches under various noise effects.

and this section focuses on two primary types: (1) noise introduced into the excitation signal (i.e., external wave load on the structure), and (2) noise added to the response signal (i.e., the acceleration measured by the sensor). In the first case, the influence of ambient noise on the external load of the structure is simulated, and the structural response is recorded using an error-free acceleration sensor. In the second case, ambient noise is simulated in the sensor data, assuming the input signal remains accurate. This section explores both cases in detail and compares the results with those obtained from traditional methods, providing a comprehensive understanding of how noise impacts the proposed method.

The impact of noise in the input signal is first examined to assess the accuracy of motion response reconstruction when the input load is contaminated with noise. The external load on the 6-DOF of the structure is derived from Orcaflex simulations. While Orcaflex provides an idealized model of the external load during structural motion, real-world external loads are often influenced by mechanical vibrations, environmental noise, and other disturbances. These real-world factors are not captured in the Orcaflex calculations, which can lead to discrepancies when comparing the calculated external loads to those observed on actual offshore structures. To simulate external noise pollution in the load, Gaussian white noise $n(t)$, is added to the structural load $f(t)$, yielding a contaminated load, $f^*(t) = f(t) + \alpha f(t)$, where α represents the noise level. The external loads acting on the 6-DOF of the structure are then corrected accordingly. Figure 4a illustrates the original external loads, alongside the results after contamination with Gaussian white noise of varying intensities.

By incorporating the noise-corrected external load into Orcaflex, the dynamic response of the structure can be recalculated. Figure 4b shows a comparison of the calculated heave acceleration and displacement under 0% and 30% noise levels. The results reveal that the structural acceleration and displacement differ when the external load is influenced by noise, compared to when it is unaffected. This discrepancy is attributed to the impact of noise on the input signal, leading to variations in the calculated acceleration and displacement at different noise levels. Figure 4 provides a quantitative evaluation of the reconstructed displacement using the proposed method under various noise levels (0%, 5%, 10%, 15%, 20%, 25%, and 30%), represented by Original, Noise-5, Noise-10, Noise-15, Noise-20, Noise-25, Noise-30. The results show that, among the five approaches, the polynomial-based and filter-based approaches exhibit negative or near-zero correlation coefficients due to phase errors, leading to more pronounced amplitude discrepancies. In contrast, the proposed method consistently outperforms traditional approaches in both correlation and amplitude accuracy, achieving high-precision displacement reconstruction even under increasing noise levels.

The second case examines the impact of adding varying levels of Gaussian white noise to the calculated acceleration signal, which is then used to reconstruct the displacement of the structure. Before the analysis, the acceleration signal is modified as follows: $\ddot{x} * (t) = \ddot{x}(t) + \alpha\ddot{x}(t)$. Figure 5a, b shows the time- and frequency-domains results of heave acceleration with different intensities of Gaussian white noise. In this scenario, the error in displacement reconstruction arises from the noise introduced into the output signal. The noise-affected acceleration signal is then used for displacement reconstruction. The evaluation results for various methods are presented in Fig. 5c. These results reveal that, in comparison to traditional approaches, the proposed method offers superior performance in both correlation and amplitude accuracy, demonstrating its robustness and suitability for displacement reconstruction in offshore floating structures, even in environments with substantial noise interference.

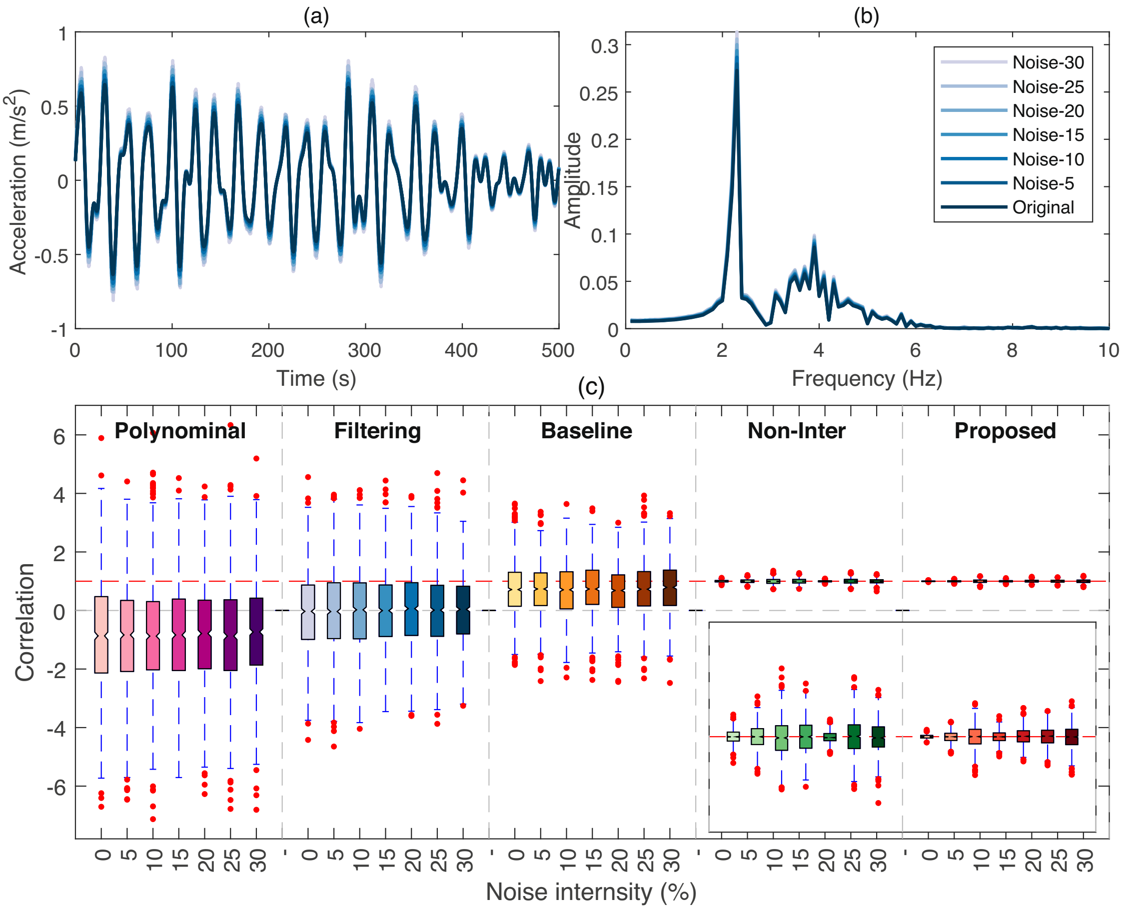

Fig. 5 | Displacement reconstruction under the second noise interference condition. Calculated acceleration affected by varying noise levels in the (**a**) time and (**b**) frequency domains. **c** Quantitative evaluation results of displacement reconstructed by different approaches under various noise effects.

Application to a physical model of the semi-submersible platform

To validate the accuracy of the proposed method experimentally, laboratory tests were conducted using a 1/100 scale model of the semi-submersible platform (as shown in Supplementary Fig. 4). These tests were carried out in both an indoor wave flume and an outdoor pool. The reconstructed displacement results obtained from the proposed method were then compared with those from commonly used measurement devices, including the optical system and the INS/DGPS system. Due to the influence of marine environment and distance from the base station on the testing accuracy of INS/GPS system, its testing accuracy cannot be directly used to prove the correctness of the reconstruction results of this method. Therefore, in the experiment, we used an optical system to provide a standard answer for the reconstruction results, as the testing accuracy of the optical system can reach the millimeter level.

Displacement testing under indoor pool conditions. First, the semi-submersible platform was positioned in a wave flume measuring 60 m × 3.0 m × 1.5 m. A piston-type wave generator, capable of simulating both regular and irregular waves with generation periods ranging from 1 to 3 s and a maximum wave height of 0.2 m, was fixed at the end of the wave flume. The motion response of the structure was measured using an accelerometer and an optical 6-DOF system. The accelerometer model used was MEAS 4803A-0002C000488, and the recorded response were capture by a 16-channel IMC acquisition instrument. The optical 6-DOF system was developed using the commercial HTC Vive Pro kit, which consists of one onshore base station and two onboard markers. The system offers a maximum sampling frequency of 4630 Hz and a measurement accuracy of 0.01 mm. The layout of the platform and the associated devices are shown in Supplementary Fig. 4. Due to the limited simulation range of the wave generator, a total of 5 wave periods (1.2 s, 1.6 s, 2.0 s, 2.4 s, 2.8 s) and three wave heights (0.06 m, 0.09 m, 0.12 m) were selected for conducting regular and irregular wave tests, resulting in a total of 15 sets of operational conditions.

Irregular waves, simulated using the JONSWAP spectrum with a significant wave height of 0.12 m and a spectral peak period of 2 s, were used to excite the platform. The recorded heave accelerations, sampled at a frequency of 50 Hz, are shown in Fig. 6a. For the analysis, data from 500 to 650 s were selected to verify the displacement reconstruction. To reconstruct the structural displacement using the proposed method, the measured acceleration was first integrated. The displacement resulting from this integration was characterized using the proposed method, yielding 75 groups of conjugate characterization parameters, including 23 groups of components with frequencies below 0.1 Hz, as shown in Fig. 6b. The actual structural displacement was then reconstructed using the remaining parameters, and the results are presented in Fig. 6c. For comparison, the figure also presents the reconstructed displacement using the Non-integral approach. Based on the analysis, both the Non-integral approach and the proposed method demonstrated clear advantages over the other three approaches, so these methods will not be included in the following comparisons. The time-domain results indicate that the displacement reconstruction from the proposed method aligns more closely with the test results obtained from the optical system.

To further compare the Non-integral approach with the proposed method, a comparative analysis was performed from the perspectives of computational efficiency and computational time scale, with the results presented in Fig. 6d. As shown in the figure, under the same modal order, the calculation time of the Non-integral approach increases exponentially with the time scale, surpassing that of the proposed method. Additionally, the

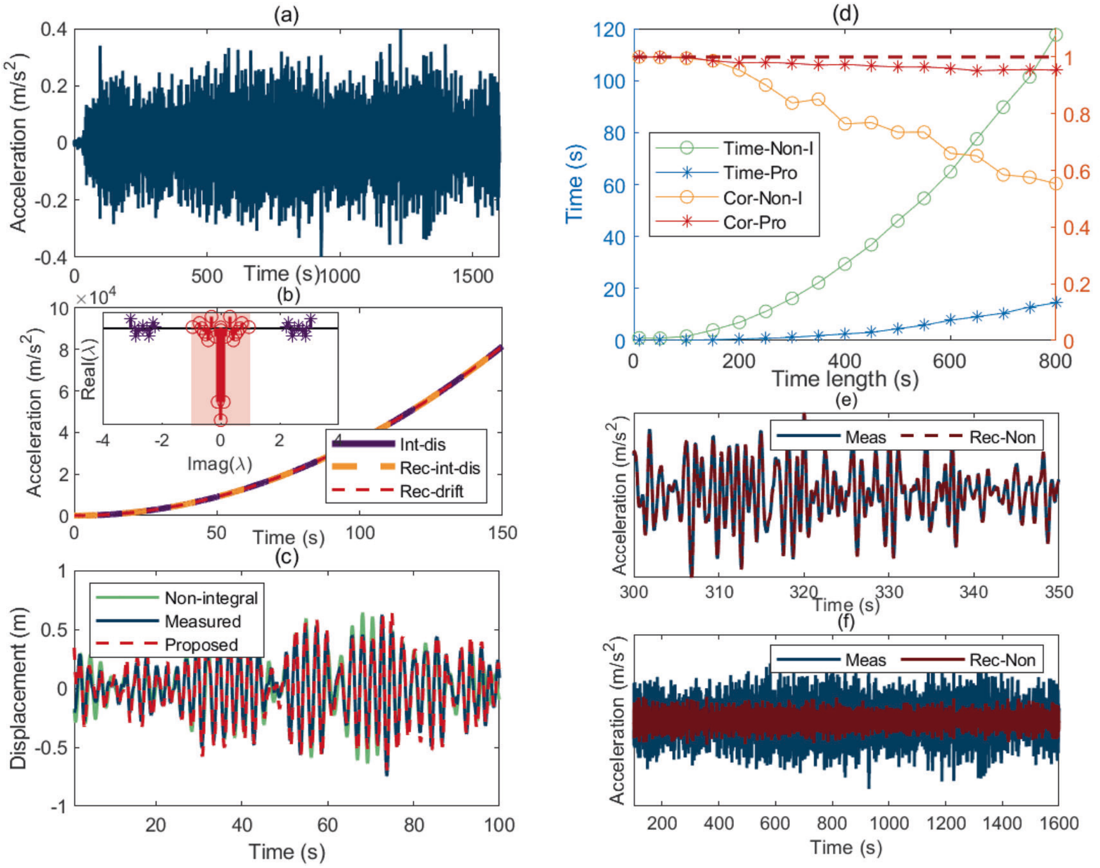

Fig. 6 | Displacement reconstruction results of the indoor experiment. **a** Measured acceleration. **b** Comparison of the integrated displacement, reconstructed integrated displacement, and reconstructed drift terms. **c** Comparison of measured displacement and the proposed method. **d** Quantitative evaluation of the reconstructed displacement; Comparison of measured and reconstructed acceleration by the Non-integral approach over a duration of (**e**) 50 s and (**f**) 1500 s.

accuracy of the reconstruction results shows a noticeable decline, as its decomposition accuracy heavily depends on the selected modal order. Figure 6e, f presents the comparative results of acceleration reconstruction using the Non-integral approach at the same modal order. For shorter time scales (50 s), the reconstruction results are relatively better, but for longer time scales (1600 s), the reconstruction quality deteriorates. This ill-conditioned behavior may severely affect the application of the Non-Integral approach to measured data from offshore floating structures, as selecting the correct modal order becomes increasingly difficult due to the interference of complex components. In contrast, both the computational efficiency and accuracy of the proposed method remain stable across time scales. The inherent advantages of integration in the proposed method reduce the structures sensitivity to high-frequency noise, effectively mitigating its impact on the motion response.

Then, the measured acceleration of the structure obtained under different marine environments is used to reconstruct the motion displacement, and the error between the reconstructed displacement and the measured displacement by the optical system are quantitatively evaluated using Eqs. (18) and (19). The results are shown in Fig. 7a. Figure 7b–d shows the time-domain comparison of reconstructed displacement and measured displacement. It can be seen that the correlation coefficient between the reconstructed displacement and the measured displacement of the proposed method is above 99%, and the maximum normalization error is below 30%, with error accuracy in the mm level, which verifies the applicability of the proposed method in different marine environments.

Displacement testing under outdoor pool conditions. Since the satellite signal for the DGPS system would be obstructed in the sheltered indoor wave flume, rendering the INS/DGPS system unusable, the platform was relocated to an outdoor pool (10 m × 5 m × 1 m) with no shelter for comparison purposes. During this outdoor testing, an accelerometer and an INS/DGPS system (model SDI-INS 100) were installed on the platform, as shown in Supplementary Fig. 5. To validate the accuracy of the comparison results, the optical 6-DOF system was also employed as a reference measurement. The test, however, highlighted the limitation of the optical system: excessive ambient light in open environments led to data loss, particularly during daylight conditions. To address this, a light mask was constructed to mitigate this issue. Furthermore, due to the lack of a wave generator in the outdoor pool, simulating real marine conditions was not feasible. As a result, two experimental scenarios were considered: simple heave-free attenuation and artificial wave testing.

In the experiment, the heave-free motion was simulated by applying a vertical force to the floating platform. The measured acceleration is presented in Fig. 8a. As illustrated in the figure, the structure was released at 28 s, began to move, and stabilized after 60 s. Therefore, acceleration data from 28 s to 60 s were selected for further analysis. First, the measured acceleration was integrated, followed by the characterization of the integral displacement, as shown in Fig. 8b. After removing frequencies below 0.1 Hz, the resulting reconstructed displacement is depicted in Fig. 8c. A comparison with the test results from the DGPS, GPS-INS system, and the optical system is also provided. It is evident that the small motion amplitude of the model structure makes the direct use of DGPS unsuitable for the test. While combining DGPS with INS improves accuracy, it introduces a drift issue over time. In contrast, the reconstructed displacement using the proposed method closely matches the measurements from the optical 6DOF system, achieving millimeter-level accuracy. This further demonstrates the superiority of the proposed method for structural displacement measurement in real-world marine environments.

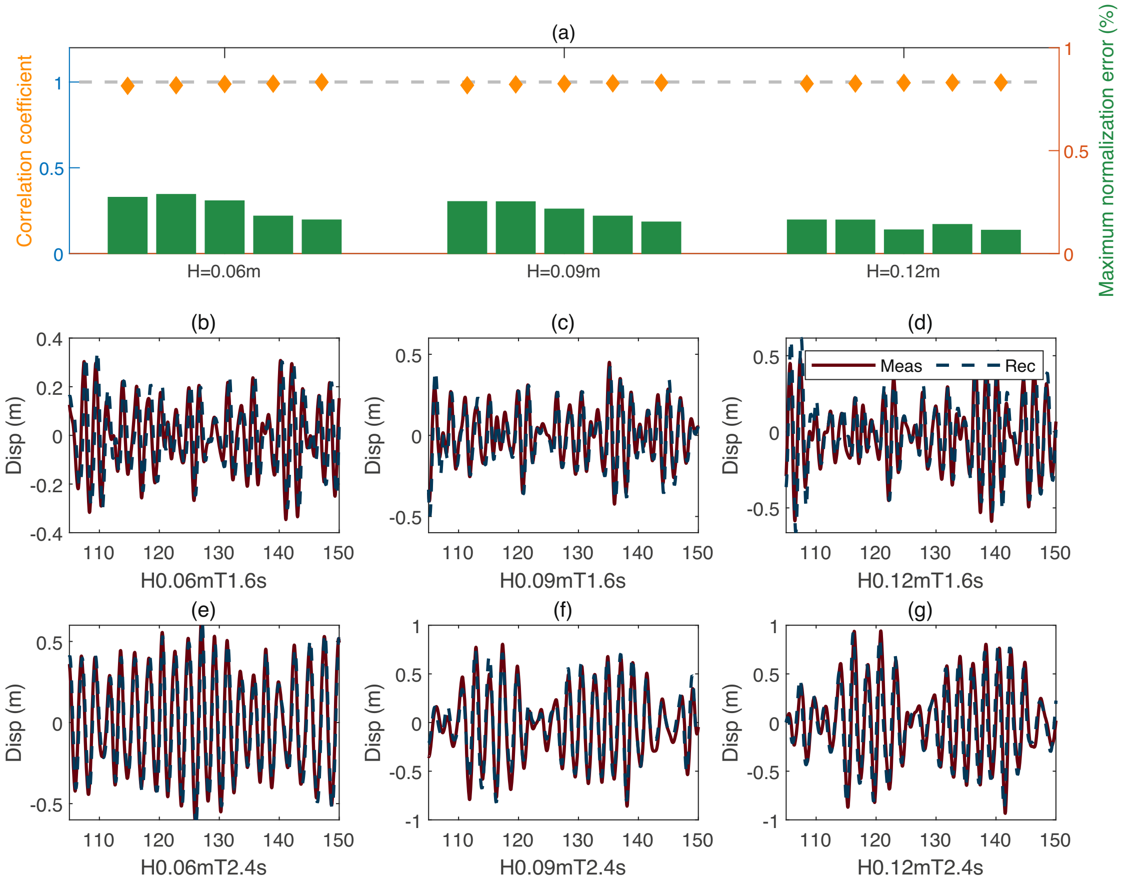

Fig. 7 | Quantitative evaluation with different wave heights and periods. a Quantitative evaluation of the errors. Reconstructed displacement in the time domain: (**b**) 0.06 m and 1.6 s; (**c**) 0.09 m and 1.6 s; (**d**) 0.12 m and 1.6 s; (**e**) 0.06 m and 2.4 s; (**f**) 0.09 m and 2.4 s; (**d**) 0.12 m and 2.4 s.

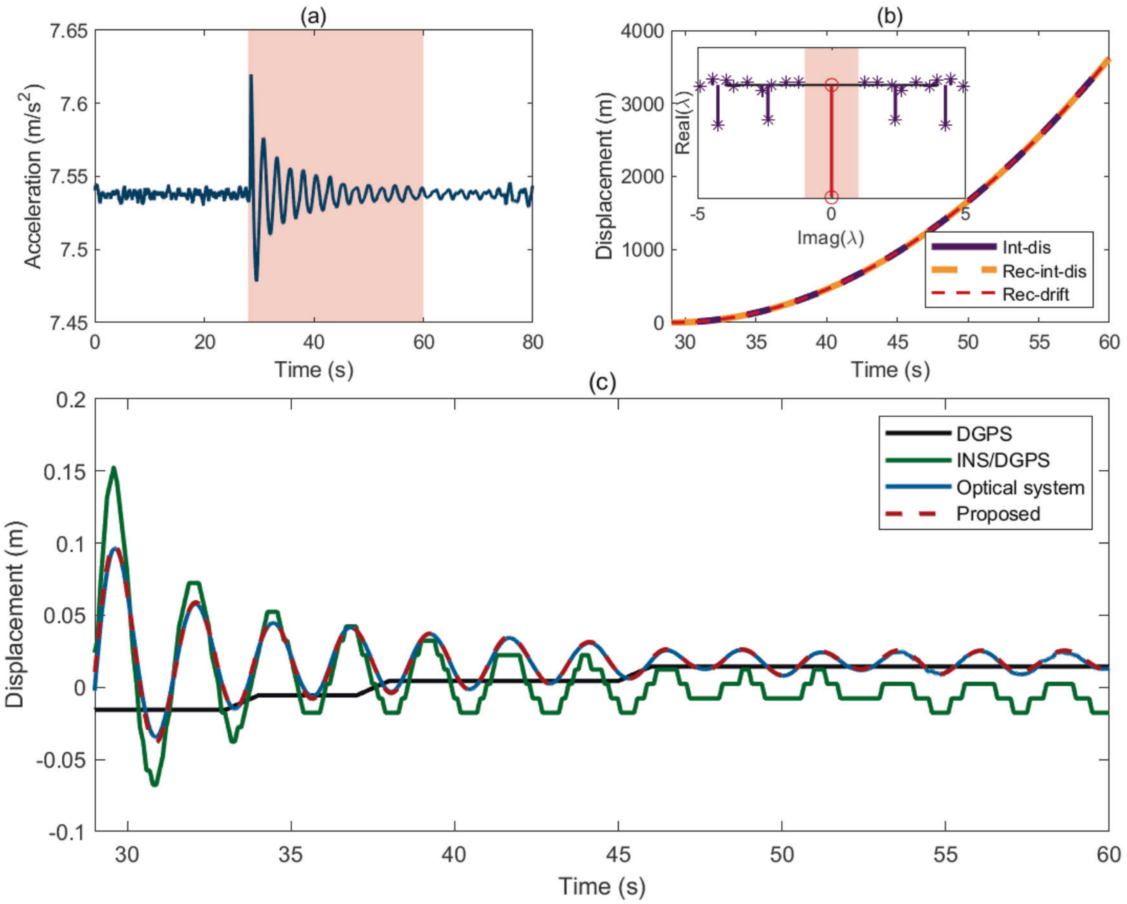

Fig. 8 | Displacement reconstruction results of the heave-free motion case of the outdoor experiment. a Measured acceleration. **b** Comparison of integrated displacement, reconstructed integrated displacement, and reconstructed drift terms. **c** Comparison of measured displacement with the reconstructed displacement.

The second experiment aimed to simulate irregular waves through artificial excitation. The test results obtained using the INS/DGPS system, the proposed method, and the optical system are illustrated in Fig. 9a. As shown in the figure, the artificial wave excitation results in a vertical motion amplitude only reach a few millimeters, which is below the measurement capability of the INS/DGPS system. In contrast, the displacement reconstruction results from the proposed method align with the measurements obtained from the optical system.

Another noteworthy phenomenon observed during the experiments was the occurrence of breakpoints in the measured results from the optical 6-DOF system, indicating data loss, as shown in Fig. 9(a). To investigate the causes of these breakpoints, Fig. 9b presents the statistics of data loss percentage under conditions of free motion, regular waves, and random waves, both in the indoor flume and outdoor pool. The results show that in the indoor flume, the percentage of data loss due to random waves is the highest, reaching up to 10% in severe cases. The data loss can be attributed to the working principle of the optical 6DOF tracking system, which requires capturing marker points on the structure to accurately track its motion. If the amplitude of the structural motion exceeds the capture range of the system's camera, the marker points may be obscured, leading to data loss. Additionally, the problem of data loss is more pronounced in the outdoor pool conditions, where the loss rate can reach nearly 50%. This issue is primarily caused by the unrestricted horizontal movement of the structure in the outdoor pool, as there is no mooring system to limit its range of motion. Consequently, the structure's motion often exceeds the area covered by the optical system's cameras. Moreover, strong ambient light in outdoor environments can interfere with the optical system, preventing it from effectively tracking the marker points. As an example, Fig. 9c compares the results reconstructed by the proposed method with measurements from the optical 6-DOF system during a test with nearly 50% data loss. The figure demonstrates that during periods of data loss (from 58 to 102 s), the optical system fails to capture the motion, but the proposed method successfully estimates the heave response. In contrast, from 36 to 58 s and 102 to 108 s, where the optical system provides reliable data, the proposed method's reconstructed results closely align with the measured data, confirming its robustness and accuracy.

Application to field test data

This section presents field tests conducted on a real offshore wind power installation platform in a marine environment to evaluate the performance of the proposed method in comparison with traditional approaches and the INS/DGPS system. The objective is to verify the effectiveness of the proposed method in addressing the challenges associated with floating structures in engineering applications. The sea trials were conducted in areas near Yantai, China, on a platform shown in Supplementary Fig. 6. The platform measures 126 m in length, 50 m in width, and 10 m in depth, with an installation capacity of over 10 MW for offshore wind turbines. This design is tailored to meet the growing demands of large-scale offshore wind power construction operations. During the tests, acceleration sensors and INS/DGPS systems were installed at key locations, including the bow, stern, and deck, to monitor the platform's structural movement.

Comparison to the measuring equipment

Figure 10a shows the measured heave acceleration, while Fig. 10b presents the displacement data recorded by the INS/DGPS system. It

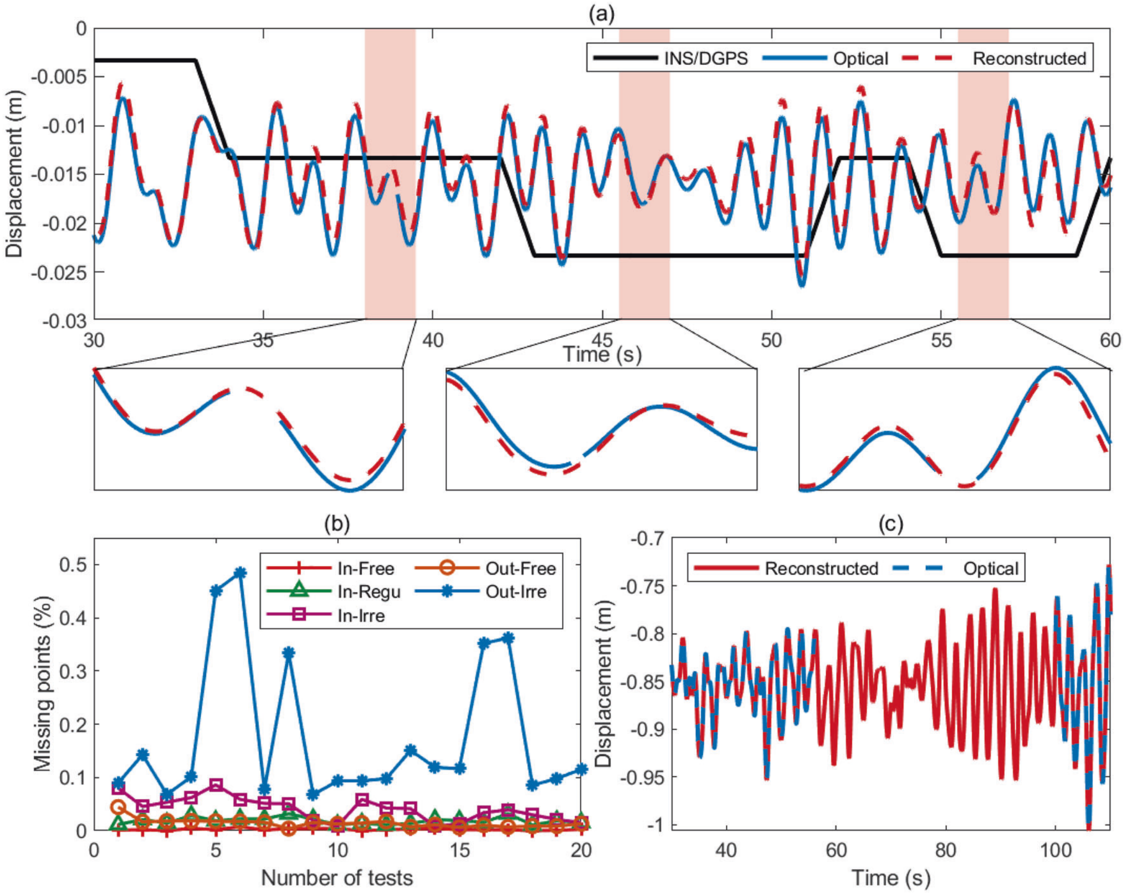

Fig. 9 | Displacement reconstruction results of the irregular wave case of the outdoor experiment. (**a**) Comparison of measured and reconstructed displacement. **b** Statistical analysis of missing data points under different conditions. **c** Comparison of measured and reconstructed displacement with 50% data loss.

is observed that the data from the INS/DGPS system is slightly affected by baseline drift over short periods, but this influence becomes more pronounced over longer durations. To minimize drift, data from 100 to 400 s were selected for further analysis. Figure 10d compares the reconstructed displacement by the proposed method with the DGPS measurements. The results show that the displacement reconstruction using the proposed method successfully tracks the platforms motion, closely aligning with the DGPS measurements. However, due to the lower sampling frequency of the DGPS, much of the detailed structural motion information can not be captured. This highlights that the proposed method not only captures detailed motion information with high accuracy, but also effectively mitigates the drift issues commonly associated with DGPS, making it a more reliable solution for real-time motion tracking of floating structures.

Comparison to traditional methods

Figure 10e–h presents the reconstructed displacements obtained using traditional approaches, along with the corresponding assessment results (Fig. 10c). It is clear that traditional approaches fail to accurately capture the operational behavior of the structure during actual ship tests, with maximum errors exceeding 100% and similarity indices below 50%. In contrast, the displacement reconstruction results obtained using the proposed method show better alignment with the test data from the INS/DGPS system, achieving a similarity index of 85.71% and a maximum error of 30.97%. However, it is important to note that these results do not suggest low amplitude accuracy for the proposed method. The limited accuracy of the INS/DGPS system in the heave direction means its data should be considered as a reference rather than an exact measurement. Based on the previous analysis and the comparative results with the optical 6DOF system from the experiment, it can be concluded that the proposed method achieves millimeter-level accuracy, surpassing the accuracy of the INS/DGPS system, and demonstrates strong potential for reliably estimating heave motion in floating structures.

Conclusions

In this paper, a displacement reconstruction method that accurately reconstructs the motion response of floating structures in deep-sea environments by precisely removing drift terms is proposed. The method integrates acceleration data and identifies drift terms through normalized representation and frequency screening. Simulation results from Orcaflex, modeling a semi-submersible platform under various marine environmental factors and equipment conditions, demonstrate that the reconstruction results from the proposed method align closely with the calculated data. These results show higher accuracy and greater robustness compared to traditional approaches, achieving reliable estimation of the initial conditions of structural motion.

To further validate the feasibility of this method for complex ocean structures, tests were conducted on a 1:100 scale semi-submersible platform and a real offshore platform. The proposed method's error, when compared to the optical 6DOF system, was limited to millimeter-level accuracy. The Pearson correlation coefficient of the displacement reconstruction reached 96.62%, with a maximum normalization error of 6.12%. Additionally, analysis of data from outdoor pool experiments and real ship tests reveals that, compared to commonly used displacement measurement tools (such as the optical 6DOF system and the INS/DGPS system), the proposed method exhibits superior resistance to environmental interference and data

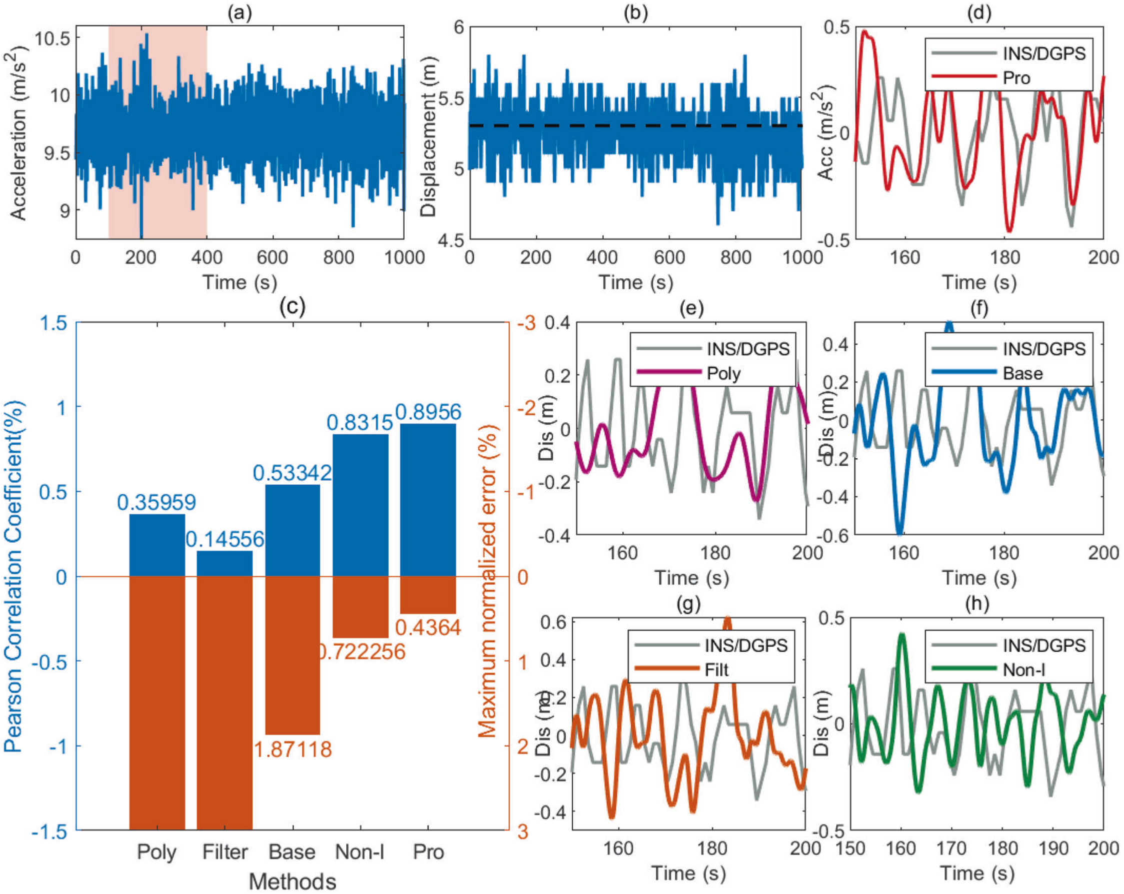

Fig. 10 | Displacement reconstruction of the field test. Measured (**a**) acceleration and (**b**) displacement in the time domain. **d**–**h** Comparison of the measured displacement with the reconstructed displacement. **c** Quantitative evaluation results of the reconstructed displacement.

loss, delivering excellent performance and higher accuracy. It must be acknowledged that this work is related to heave response, while surge/sway response is more complex and can be affected by devices such as thrusters and propellers, resulting in uniform or quasi-uniform motion. This may lead to the absence of acceleration characteristics in the structural surge/sway response. Therefore, it is impossible to reconstruct the displacement of the structure through acceleration characteristics. In future research, we also hope to overcome this limitation and achieve horizontal motion response reconstruction of structures not based on INS/GPS systems.

Data availability

All data used in this research are available from the corresponding authors upon reasonable request.

Code availability

All codes used in this research are available from the corresponding authors upon reasonable request.

Received: 7 November 2024; Accepted: 25 March 2025;

References

1. Anghel, A. et al. Compact ground-based interferometric synthetic aperture radar short-range structural monitoring. *IEEE Signal Process. Mag.* **36**, 42–52 (2019).
2. Yangm, L. et al. Large-amplitude rotation of floating offshore wind turbines: a comprehensive review of causes, consequences, and solutions. *Renew. Sust. Energy Rev.* **211**, 115295 (2025).
3. Kim, K. Y. & Sohn, H. Dynamic displacement estimation by fusing LDV and LiDAR measurements via smoothing based Kalman filtering. *Mech. Syst. Signal Process.* **82**, 339–355 (2017).
4. Gao, S. J., Feng, G. N. & Liu, F. S. Investigation to the nonlinearity evolution of offshore wind turbines using field data: Application to a 4 MW monopile offshore wind turbine. *Appl. Ocean Res.* **145**, 103918 (2024).
5. Dong, X. F., Lian, J. J., Wang, H. J., Yu, T. S. & Zhao, Y. Structural vibration monitoring and operational modal analysis of offshore wind turbine structure. *Ocean Eng.* **150**, 280–297 (2018).
6. Dong, X. F., Lian, J. J. & Wang, H. J. Vibration source identification of offshore wind turbine structure based on optimized spectral kurtosis and ensemble empirical mode decomposition. *Ocean Eng.* **172**, 199–212 (2019).
7. Mastronardi, N., Kressner, D., Sima, V., Dooren, P. V. & Huffel, S. B. A fast algorithm for subspace state-space system identification via exploitation of the displacement structure. *J. Comput. Appl. Math.* **132**, 71–81 (2001).
8. Feng, D. M. & Feng, M. Q. Identification of structural stiffness and excitation forces in time domain using noncontact vision-based displacement measurement. *J. Sound Vib.* **406**, 15–28 (2017).
9. Hamedani, S. J. & Khedmati, M. R. Optimized planning for weather-sensitive offshore construction operations—an application to float-over installation of super-heavy offshore topsides. *Ocean Eng.* **297**, 117027 (2024).
10. Kim, S., Park, K.-Y., Kim, H.-K. & Lee, H. S. Damping estimates from reconstructed displacement for low-frequency dominant structures. *Mech. Syst. Signal Process.* **136**, 106533 (2020).

11. Zhu, H., Zhou, Y. J. & Hu, Y. M. Displacement reconstruction from measured accelerations and accuracy control of integration based on a low-frequency attenuation algorithm. *Soil. Dyn. Earthq. Eng.* **133**, 106122 (2020).
12. Kim, J., Kim, K. Y. & Sohn, H. Autonomous dynamic displacement estimation from data fusion of acceleration and intermittent displacement measurements. *Mech. Syst. Signal Process.* **42**, 194–205 (2014).
13. Gao, S. J., Feng, G. N., Liu, D. Z. & Liu, F. S. Separation and quantitative evaluation for the nonlinear effects in the motion response of floating structures. *Ocean Eng.* **301**, 117549 (2024).
14. Gao, S. J., Liu, F. S., Chang, S. & Zhou, L. A dynamic response analysis method with high-order accuracy for fixed offshore structures based on a normalised expression of external loadings. *Ocean Eng.* **219**, 108358 (2021).
15. Adali, T. An exciting juncture for signal processing research: on building bridges, challenges, and opportunities. *IEEE Signal Process. Mag.* **41**, 3–6 (2024).
16. Kwiatkowski, J., Anigacz, W. & Beben, D. A case study on the noncontact inventory of the oldest European cast-iron bridge using terrestrial laser scanning and photogrammetric techniques. *Remote Sens.* **12**, 2745 (2020).
17. Gonzlez, C. L. & Valls, P. G. D scanning methodology: bell tower of Santa Mar de Darocas church (Spain). *ISPRS Arch.* **44**, 373–379 (2020).
18. He, Z. Z., Zhang, L. X., Gao, H. G., Wang, H. S. & Pan, P. Estimation of the displacement time history of high-rise building structures using limited measurement data and structural information. *Mech. Syst. Signal Process.* **202**, 110716 (2023).
19. Fu, Y. B. et al. Analytical solution to the mechanical response of grouting lifting in existing shield tunnels and engineering case verification. *Tunn. Undergr. Sp. Tech.* **145**, 105587 (2024).
20. Li, J. C., Huang, M. L. & Zhao, Z. Y. Mechanical response and field measurement analysis of custom-shaped steel sleeves during urban shield tunnel construction. *Tunn. Undergr. Sp. Tech.* **143**, 105483 (2024).
21. Assefa, S., Graziani, A. & Lembo-Fazio, A. A slope movement in a complex rock formation: deformation measurements and DEM modelling. *Eng. Geol.* **219**, 74–91 (2017).
22. Wang, H. F. et al. A slope deformation measurement method based on laser datum and complex target motion model. *Measurement* **199**, 111526 (2022).
23. Wei, D. T., Chen, Y. G., Li, H. K. & Zhang, X. W. Real-time reconstruction method of full-field dynamic response of rotating bladed disks. *Mech. Syst. Signal Process.* **188**, 109953 (2023).
24. Damaris, A. L. & Jaime, D. L. C. Assessment of methodologies to estimate displacements from measured acceleration records. *Measurement* **114**, 261–273 (2018).
25. Shen, C. et al. Multi-rate strong tracking square-root cubature Kalman filter for MEMS-INS/GPS/polarization compass integrated navigation system. *Mech. Syst. Signal Process.* **163**, 108146 (2022).
26. Wu, Q. W., Pan, Y. H., Ding, H., Xiao, Y. X. & He, X. X. Quantifying the effect of non-seasonal non-tidal loadings on background noise properties of GPS vertical displacements in mainland China. *Measurement* **217**, 113007 (2023).
27. Teigen, P. & Haver, S. The heidrun TLP: measured versus predicted response. *Appl. Ocean Res.* **20**, 27–35 (1998).
28. Liagre, P., Gupta, H. & Banon, H. Monitoring of floating offshore installations wave frequency motions. In *Proc. Offshore Technology Conference* (OnePetro, 2008).
29. Granados, G. S., Salcedo, J. A. L., Banos, D. J. & Risueno, G. L. Challenges in Indoor Global Navigation Satellite Systems unveiling its core features in signal processing. *IEEE Signal Process. Mag.* **29**, 108–131 (2012).
30. Nezhadshahbodaghi, M. & Mosavi, M. R. A loosely-coupled EMD-denoised stereo VO/INS/GPS integration system in GNSS-denied environments. *Measurement* **183**, 109895 (2021).
31. Jaime, D.-L.-C., Damaris, A.-L. & Jesús, V.-G. Effect of noise on the assessment of displacements computed from accelerations recorded at linear and nonlinear civil engineering structures. *Measurement* **136**, 724–734 (2019).
32. Trifunac, M. D. & Lee, V. M. *Routine Computer Processing of Strong-motion Accelerograms*. 73-03 (California Institute of Technology, Earthquake Engineering Research Laboratory Pasadena, California, EERL, 1973).
33. Converse, A. & Brady, A. G. BAP basic strong-motion accelerogram processing software version 1.0, United States Department of the Interior, U.S. Geological survey; Distributed by Books and Open-file Reports Section. USGS Numbered Series 92-296-A (1992).
34. Wang, W. Y. & Dogancay, K. Widely linear adaptive filtering based on clifford geometric algebra: a unified framework. *IEEE Signal Process. Mag.* **41**, 86–101 (2024).
35. Park, K.-T., Kim, S.-H., Park, H.-S. & Lee, K.-W. The determination of bridge displacement using measured acceleration. *Eng. Struct.* **27**, 371–378 (2005).
36. Wang, R., Schurr, B., Milkereit, C., Shao, Z. & Jin, M. An improved automatic scheme for empirical baseline correction of digital strong-motion records. *Bull. Seismol. Soc. Am.* **101**, 2029–2044 (2011).
37. Gao, S. J., Liu, F. S. & Jiang, C. Y. Improvement study of modal analysis for offshore structures based on reconstructed displacements. *Appl. Ocean Res.* **110**, 102596 (2021).
38. Chiu, S. W. & Parhi, K. K. Long polynomial modular multiplication using low-complexity number theoretic transform. *IEEE Signal Process. Mag.* **41**, 92–102 (2014).
39. Gao, S. J. & Liu, F. S. Research on non-stationary characteristic test and decomposition for dynamic response of floating structures. *Ocean Eng.* **292**, 116550 (2024).
40. Liu, F. S., Gao, S. J. & Chang, S. Displacement estimation from measured acceleration for fixed offshore structures. *Appl. Ocean Res.* **113**, 102741 (2021).
41. Liu, F. S., Gao, S. J., Liu, Y. & Liu, D. Z. A motion tracking approach to position marine floating structures based on measured acceleration and angular velocity. *Ocean Eng.* **257**, 111682 (2022).
42. Roonizi, A. K. Fourier analysis: a new computing approach. *IEEE Signal Process. Mag.* **40**, 183–191 (2023).
43. Dizon, D. N. & Hogan, J. A. Holistic processing of color images using novel quaternion-valued wavelets on the plane: a promising transformative tool. *IEEE Signal Process. Mag.* **41**, 51–63 (2024).
44. Chiu, H. C. Stable baseline correction of digital strong-motion data. *Bull. Seismol. Soc. Am.* **87**, 932–944 (1997).
45. Javaid, S., Li, D. Y. & Ukil, A. Transient analysis method using high pass filter circuit in VSC interfaced multi-terminal DC system. *Electr. Pow. Syst. Res.* **216**, 109062 (2023).
46. Pieper, A. et al. High-performance implementation of Chebyshev filter diagonalization for interior eigenvalue computations. *J. Comput. Phys.* **325**, 226–243 (2016).
47. Liu, F. S., Gao, S. J., Liu, D. Z. & Zhou, H. A signal decomposition method based on repeated extraction of maximum energy component for offshore structures. *Mar. Struct.* **72**, 102779 (2020).
48. Liu, F. S., Gao, S. J., Tian, Z. & Liu, D. Z. A new time-frequency analysis method based on single mode function decomposition for offshore wind turbines. *Mar. Struct.* **72**, 102782 (2020).

Acknowledgements

The authors acknowledge the financial support of the National Natural Science Foundation of China (52125106, 52201340, U22A20243).

Author contributions

Shujian Gao: Conceptualization, Methodology, Validation, Data curation, Writing-original draft. Xi Chen: Data curation, Formal analysis. Zewen Pan: Data curation, Experiment test. Zhe Tian: Project administration. Fushun Liu: Funding acquisition.

Competing interests

The authors declare no competing interests.

Additional information

Supplementary information The online version contains supplementary material available at https://doi.org/10.1038/s44172-025-00402-9.

Correspondence and requests for materials should be addressed to Shujian Gao.

Peer review information *Communications Engineering* thanks Nianxin Ren, Xiaosen Xu, and the other, anonymous, reviewer for their contribution to the peer review of this work. Primary Handling Editors: [Anastasiia Vasylchenkova and Rosamund Daw].

Reprints and permissions information is available at http://www.nature.com/reprints

Publisher's note Springer Nature remains neutral with regard to jurisdictional claims in published maps and institutional affiliations.

Open Access This article is licensed under a Creative Commons Attribution-NonCommercial-NoDerivatives 4.0 International License, which permits any non-commercial use, sharing, distribution and reproduction in any medium or format, as long as you give appropriate credit to the original author(s) and the source, provide a link to the Creative Commons licence, and indicate if you modified the licensed material. You do not have permission under this licence to share adapted material derived from this article or parts of it. The images or other third party material in this article are included in the article's Creative Commons licence, unless indicated otherwise in a credit line to the material. If material is not included in the article's Creative Commons licence and your intended use is not permitted by statutory regulation or exceeds the permitted use, you will need to obtain permission directly from the copyright holder. To view a copy of this licence, visit http://creativecommons.org/licenses/by-nc-nd/4.0/.

© The Author(s) 2025